Biomaterials Advances 154 (2023) 213605

Contents lists available at ScienceDirect

Biomaterials Advances

journal homepage: www.journals.elsevier.com/materials-science-and-engineering-c

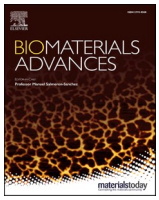

Apatite-coated outer layer eggshell membrane: A novel osteoinductive biohybrid composite for guided bone/tissue regeneration

Adriana Torres-Mansilla [a], Pedro Álvarez-Lloret [a], Ana Voltes-Martínez [b,c,d,e], Elena López-Ruiz [b,c,f,g], Paula Alejandra Baldión [h], Juan Antonio Marchal [b,c,d,e,g,*], Jaime Gómez-Morales [i,*]

[a] Department of Geology, Faculty of Geology, University of Oviedo, 33005 Oviedo, Spain
[b] Biopathology and Regenerative Medicine Institute (IBIMER), Centre for Biomedical Research (CIBM), University of Granada, 18100 Granada, Spain
[c] Instituto de Investigación Biosanitaria ibs.GRANADA, 18100 Granada, Spain
[d] Department of Human Anatomy and Embryology, Faculty of Medicine, University of Granada, 18016 Granada, Spain
[e] BioFab i3D-Biofabrication and 3D (bio)printing laboratory, University of Granada, 18100 Granada, Spain
[f] Department of Health Science, Faculty of Experimental Science, University of Jaen, 23071 Jaen, Spain
[g] Excellence Research Unit "Modelling Nature" (MNat), University of Granada, 18100 Granada, Spain
[h] Departamento de Salud Oral, Facultad de Odontología, Universidad Nacional de Colombia, 111321 Bogotá, Colombia
[i] Laboratory of Crystallographic Studies, IACT-CSIC-University of Granada. Avda. Las Palmeras, 4, 18100 Armilla, Spain

ARTICLE INFO

Keywords:
Eggshell membrane
Apatite mineralization
Vapor diffusion
Mechanical properties
Human mesenchymal stromal cells
Osteogenic differentiation
Cytocompatibility
Osteopontin
Collagen I

ABSTRACT

Hybrid biomimetic materials aim to replicate the organic-inorganic constructs of mineralized tissues. During eggshell formation, the outer surface of the eggshell membrane (ESM) promotes calcium carbonate nucleation, while the inner one prevents mineralization toward the egg white and yolk. In the current study, the outer surface of the ESM acted as a heteronucleant in calcium phosphate precipitation by the vapor diffusion sitting drop method, while the inner one remained unmineralized. The aim was to fabricate a 2D biomaterial with dual functions, osteoinductive on one side and protective against cell invasion on the other side. The microstructural, physicochemical, morphological, and mechanical properties of the mineralized ESM were characterized by XRD, TGA, XPS, FTIR/Raman, HR-SEM, and mechanical testing techniques. The cytocompatibility and osteoinductive ability were assessed by biological assays of cell viability, proliferation, and osteogenic differentiation on human mesenchymal stromal cells (hMSCs). Results indicate that the outer surface of the ESM induces the heterogeneous precipitation of carbonate-apatite phase depicting biomimetic features. In addition, the apatite/ESM shows a much higher cytocompatibility than the pristine ESM and promotes the osteogenic differentiation of hMSCs more efficiently. Overall, the apatite/ESM composite exhibits compositional, crystalline, mechanical, and biological properties that resemble those of mineralized tissues, rendering it an approachable and novel material especially useful in guided tissue/bone regeneration.

1. Introduction

Materials designed for bone and dental tissue regeneration are increasingly in demand due to the high prevalence of osteological and dental defects and the wide variety of therapies, with >2 million bone grafts performed every year [1,2]. Bone and teeth present a complex hierarchical microstructure consisting of an organic extracellular matrix mineralized with apatite nanocrystals. The role of the organic matrix is crucial since it controls the nucleation, growth, and arrangement of the apatite nanocrystals during the mineralization process [3]. Understanding these processes is essential to tackling the challenge of fabricating biomimetic materials.

Natural polymers such as cellulose, chitosan, and fibrin have been used to replicate the organic matrix in bone scaffolds [4–6]. These materials present features similar to those of the native extracellular matrix, being able to develop enhanced biocompatibility and bioactivity compared to synthetic polymers [7]. They also constitute a platform for controlling the organic-inorganic interactions during the formation of

* Corresponding authors.
E-mail addresses: UO272371@uniovi.es (A. Torres-Mansilla), pedroalvarez@uniovi.es (P. Álvarez-Lloret), elruiz@ujaen.es (E. López-Ruiz), pabaldione@unal.edu.co (P.A. Baldión), jmarchal@go.ugr.es (J.A. Marchal), jaime@lec.csic.es (J. Gómez-Morales).

https://doi.org/10.1016/j.bioadv.2023.213605
Received 9 February 2023; Received in revised form 23 August 2023; Accepted 25 August 2023
Available online 26 August 2023

the mineralized tissues. Furthermore, their specific organic-inorganic arrangement at the microstructural level and their hierarchical architecture are responsible for the physicochemical and mechanical characteristics of bone and tooth [8]. Synthetic stoichiometric hydroxyapatite has several limitations as biocompatible material since it has low solubility and chemical reactivity within biological environments and lacks structural development at different scales [9]. In contrast, biological apatite is characterized by its high solubility, nanocrystalline properties, and hierarchical organization within the tissue [8,10,11]. In bone tissue, the main components that constitute the organic matrix are type I collagen, non-collagenous proteins, and small organic molecules such as citrate [12], being the apatite-mineralized self-assembled collagen the structural building unit of this tissue. Knowing the strategies of bone mineralization provides us with a source of inspiration to develop novel biomimetic hybrid apatite-based materials intended for tissue regeneration.

Eggshell mineralization comprises a mineral component, mainly calcium carbonate of calcite phase, coupled to the outer surface of a membrane [13]. The eggshell membrane (ESM) acts as a biopolymer network in the shell mineralization during oviproduction, promoting the precipitation of the mineral in <24 h [14]. The fibers of the ESM are composed of collagens (I, V, and X) (around 10 % of the total protein content) [15], glycosaminoglycans, egg white proteins, and eggshell matrix proteins, with collagens forming the core of the fibers [16]. The ESM is a triple-layer structure formed by the outer membrane, closer to the shell, the inner layer-intertwined with fibers in the outer membrane–, and the limiting membrane –covering the egg white [17]. The core of fibers of the outer membrane is mainly composed of collagen I, while those of the innermost membrane present collagens I and V [18], with an estimated ratio between type I and type V collagens to be close to 100:1 [19]. Type X collagen is also present in the core of fibers of both layers. The outer layer of the ESM, with a 50–70 μm thickness, contains dense nodules known as "mammillary knobs" (referred to as mammillary nuclei or "mammillae"), rich in a highly sulfated proteoglycan called "mamillan" which allows a strong binding to the shell on its inner side [20]. In these mammillary knobs, the first calcium carbonate nuclei are formed, thus initiating the shell mineralization during the process of oviproduction [20]. In addition, it was reported that ESM acts as a barrier to prevent inward mineralization toward the egg white and yolk [21]. Thus, the outer layer of the membrane is a suitable heteronucleant surface for its application in the controlled synthesis of nanocrystalline calcium phosphate apatite.

ESM has been used to induce the heterogeneous precipitation of either flower-like, spherical, or needle-shape apatite crystals by treating the membrane *via* simple diffusion [22], sodium trimetaphosphate [23], or simulated body fluid (SBF) [24], respectively. In the last method, the ESM was extracted in an acidic medium (HCl 1 M), and the biomimetic mineralization of ESM immersed in simulated body fluid (SBF) took place on both sides of the membrane. Only this research reported *in vitro* biological tests and demonstrated the enhanced osteogenic activity of the mineralized membrane [24].

Guided bone/tissue regeneration is widely used in dentistry to aid in regenerating bone/tissue at a defective location [25]. The role of membranes made either of natural (collagen, chitosan, gelatin [26], or synthetic resorbable polymers such as polylactic acid (PLA), polyglycolic acid (PGL), and their copolymers [27], is to act as an effective physical barrier between the gingival soft tissue and the bone tissue, preventing the bone graft area from external cell invasion, and serving as a scaffold for new bone formation [27]. Exploiting the ESM to build a hybrid organo-mineral material with a dual function, *i.e.*, bone graft material on one side and protective barrier to cell invasion on the other side can potentially be useful in this field. Moreover, the ESM presents lower-rate biodegradability, conferring longer-term stability than collagen membranes. The degradation pattern has been estimated to be around 16 weeks, which is superior to the collagen degradation pattern of around four weeks [25,28–30]. Thus, using the ESM could be useful in clinical practice to avoid further surgery to remove the membrane. In this regard, the procedure for removing ESM from the eggshell preventing damage to the mammillae, the mineralization method, and the temperature and pH during the precipitation process have a strong influence on the calcium phosphate phase, size, and crystallinity of the coating, and therefore, on the biocompatibility and the osteoinductive capacity of the biomaterial. It was demonstrated that extracting ESM in strongly acidic media and EDTA produces changes in the protein backbone structure [31], thus manual extraction was considered the best option for the envisaged application.

Different methods to achieve apatite crystallization include solid-state methods and wet-chemical syntheses such as sol-gel, co-precipitation, and hydrothermal synthesis [32]. These methodologies often require high temperatures, pH control, and long experimental times. In addition, many of them are unlikely to produce uniform nano-sized apatite crystals and complex structures on a more significant length [12]. The vapor diffusion sitting drop (VDSD) crystallization method was previously used to synthesize low-crystalline, plate-like, carbonated apatite crystals that resemble those of biological apatite [33–36]. The method consists of diffusing NH_3 and CO_2 vapors, emerging from a NH_4HCO_3 solution, through isolated aqueous droplets containing calcium-acetate complexes and hydrogen phosphate ions, thus increasing their pH and inducing the precipitation of carbonated calcium phosphate [35]. Among its advantages, the method allows for performing crystallization in microliter volumes with high reproducibility, at mild conditions, and at physiological temperatures and pHs [33–36]. The VDSD method has been previously employed for the heterogeneous nucleation of apatite on different mineral surfaces [33,37], although its application to biological membranes has not yet been explored.

Biocompatibility is one of the most critical properties for the application of tissue-engineered materials when implanted in a specific local tissue microenvironment [38,39]. To be considered biocompatible, the materials must not present toxicity or cause adverse reactions in the organism, and they must be non-carcinogenic. The mineralization of the outer layer of the ESM with a bone-like apatite layer should favor biocompatibility, osteoinduction, and osteoconduction of the membrane. At the same time, the opposite non-mineralized surface should present compatibility with cells related to epithelial and connective tissue.

The current study aims to exploit the physicochemical features of the outer surface of the ESM, populated by mammillae, to control the heterogeneous precipitation of calcium phosphate (CaP) and to build an organo-mineral biohybrid composite, leaving its opposite inner side unmineralized. For this objective, the VDSD method was used under ambient and physiological temperatures (25 °C and 37 °C, respectively) and at different experimental times. Special attention was paid to the physicochemical, morphological, microstructural and mechanical characterization of the mineralized membrane (mESM) by means of complementary analytical techniques (*i.e.*, SEM-EDX, TG, XPS, XRD, FTIR/Raman and mechanical testing). In addition, the performance of the mESM in response to biological assays was analyzed to explore its biocompatibility, as well as its osteoinductive ability on human mesenchymal stromal cells (hMSCs).

2. Materials and methods

2.1. Crystallization of calcium phosphate on the outer layer of ESM

ESMs were carefully obtained by manual peeling from the eggshell, in order to preserve the mammillary knobs of the outer surface (*i.e.*, the side of the membrane in contact with the shell). The ESM fragments were washed and sectioned into Ø 8 mm round pieces using a biopsy punch. The VDSD mineralization experiments were performed in a "crystallization mushroom" (Triana Sci. & Tech. S.L., Spain), a glass microreactor consisting of two cylindrical glass chambers connected

through a Ø 6 mm hole (Supplementary materials, Fig. S1). The round ESM pieces were placed in the upper chamber over its inner surface leaving the outer surface facing up to perform VDSD mineralization. Then, 20 μL of 50 mM Ca $(CH_3COO)_2$ and 20 μL of 30 mM of $(NH_4)_2HPO_4$ aqueous solutions were deposited on them, covering the full outer surface. The final Ca/P ratio in the mixed microdroplets was set at 5:3. In parallel, 3 mL of 40 mM NH_4HCO_3 were deposited in the lower chamber. Finally, the mushrooms were sealed with a top cap using high-vacuum silicone grease (Dow Corning). The experiments were performed at ~1 atm for 1, 7, and 15 days, both at room temperature (~25 °C) and 37 °C to obtain the mESM samples. All reagents were supplied by Sigma-Aldrich (>99.00 % pure, St. Louis, MO, USA), and solutions were prepared with ultrapure water (0.22 μS, 25 °C, Milli-Q, Millipore, Burlington, MA, USA).

2.2. Physicochemical, morphological, and microstructural characterization

XRD data were obtained by using an X-ray diffractometer (Bruker D8 DISCOVER, Billerica, MA, USA) equipped with an area detector (DECTRIS PILATUS 3100 K-A). For diffraction experiments, the working conditions were Cu $K\alpha_1$ radiation ($\lambda = 1.5418$ Å) at 50 kV and 30 mA, with a Ø 0.5 mm pinhole collimator. XRD patterns were collected from 4° to 70° (2θ), with a scan of 19 steps and 40 s/step. The samples were φ rotated at 90° angular steps (*i.e.*, 0°, 90°, 180° and 270°) to display the orientation of the crystals formed on the mESM. Data processing was performed by using X'Pert Highscore software (v.3.0 PANalytical, Almelo, The Netherlands). The average crystallite size (*i.e.* the dimension of the coherent diffraction domains) of Ap crystals was determined from the full width at half maximum (FWHM) of the (002) reflection by using the Debye-Scherrer formula (Eq. (1). [40]):

$$d = K\lambda/\beta\, cos\, \theta \quad (1)$$

In this equation d is the crystallite size (in nm), λ is the wavelength of the X-ray source ($CuK\alpha_1$, $\lambda = 1.54059$ Å), K is the Scherrer's constant assumed as 0.89, and β is the FWHM of the (002) reflection.

Thermogravimetric analyses (TGA-DSC3+, Mettler Toledo, Columbus, OH, USA) were performed under N_2 flow between 30 °C to 950 °C, at constant heating rate of 20 °C/min, to determine the organic matter (mass loss below 550 °C) and mineral contents.

For scanning electron microscopy (SEM) observations, the samples were carbon coated and inspected with a SEM microscope (Gemini, Carl Zeiss AG, Jena, Germany) equipped with an EDX microanalysis detector (INCA systems, Oxford Diffraction, Abingdon, UK). The microscope operated with an acceleration voltage of 3 kV, high vacuum ($\sim 10^{-4}$ mbar), a working distance of 5 mm, and aperture of 30 μm.

FTIR analyses were performed with a JASCO FP-6200 spectrometer (JASCO, Tokyo, Japan) equipped with an attenuated total reflectance (ATR) crystal diamond accessory. Spectra were recorded at a resolution of 1 cm^{-1} with 124 accumulations using a spectral range of 400–4000 cm^{-1}. Complementary spectroscopic characterization by Raman spectroscopy was done with a JASCO NRS-5100 Micro-Raman spectrometer (JASCO, Tokyo, Japan) using a spectral range of 400–3200 cm^{-1}. The excitation line was provided by a diode laser ($\lambda_{exc.} = 785$ nm) coupled with a Peltier cooled charge–couple device (CCD) with 1064 × 256-pixel dimension detector. Spectral analyses were conducted with curve fitting Peakfit v4.12, software (Systat Software, San Jose, CA, USA).

Additionally, X-ray photoelectron spectroscopy (XPS) measurements were carried out using a Kratos Axis Ultra-DLD spectrometer (Kratos -Shimadzu). Monochromatic Al Kα radiation was used in the constant energy mode of the analyzer with pass energies of 160 and 40 eV for the normal and high-resolution spectra, respectively. The spectra allowed for an elemental quantitative analysis and determination of elements bonding states in the outermost 10 nm of the solid surfaces. Two points were analyzed per sample. For more in-depth quantitative analysis, we used the same instrument by combining XPS analysis and Ar^+ ion sputtering during 0, 1, 4, 8, 16, and 32 min, at pickling rates of 1 nm/min.

2.3. Tensile strength tests of mESM samples

Additional ESMs were cut into 20 × 10 mm (L × W) sections using a biopsy punch and then mineralized at 25 and 37 °C for 7 and 15 days following the previous described methodology. The thickness of the membranes was measured following the protocol proposed by Strnková et al. [41], with slight modifications. The measurements were performed using a digital micrometer (Mitutoyo, Tokyo, Japan). The thickness of each ESM sample was used to calculate the cross-sectional area on which the tensile load was to be applied. 75 water-hydrated samples were divided in five test groups of 15 samples each. A Shimadzu AG-IS 5kN universal testing machine (Shimadzu, Tokyo, Japan) equipped with a 50 N load cell was used for tensile strength testing at a crosshead speed of 10 mm/min to the point of failure following the protocol suggested by ASTM D882 – 12 [42]. At the end of the procedure no signs of dehydration were observed. All tests were performed under conditions of 23 °C and 55 % relative humidity. The results were recorded with the Trapezium2® software (Microsoft Corp., Redmond, WA, USA). The tensile strength (MPa) was calculated by dividing the maximum load by the original cross-sectional area of the sample. The software recorded the elastic and plastic deformation of each membrane at the time of applying the tensile load, thus also allowing to obtain the following values for elastic deformation: $\mathcal{E}p$: strain at the proportional limit (%), and E: elastic modulus (MPa). Additionally, this test allows to determine the following values for plastic deformation to the point of failure: $\mathcal{E}u$: strain at breaking (%), and *KIc*: toughness (J/mm^2).

2.3.1. Data analysis

Data were analyzed with SPSS software, version 21.0 (SPSS, Chicago, IL, USA) using the Shapiro-Wilk test. The difference between groups on paired measures was determined using a Student's *t*-test. A *p*-value $\leq$ 0.05 was considered as statistically significant.

2.4. Cell viability assay and osteogenic characterization

2.4.1. Isolation, culture, and characterization of hMSCs

hMSCs were isolated from adipose tissue of patients that had liposuction procedure by enzymatic digestion using collagenase I (Sigma-Aldrich) after obtaining informed consent and authorization from the Ethics Committee of Clinical University Hospital of Málaga, Spain (ethic permission number: 02/022010). Characterization of hMSCs was developed as previously reported [66]. *Cells* were seeded in growth media [High-glucose Dulbecco's modified Eagle's medium without phenol red (DMEM; Sigma-Aldrich) supplemented with 10 % fetal bovine serum (FBS; Sigma-Aldrich), 100 U/mL penicillin, and 100 mg/mL streptomycin (P/S; Invitrogen Inc.)] at 37 °C in a humidified atmosphere with 5 % CO_2. The medium was changed every 2 days when cells reached 80 % of confluence, they were subcultured. For all the experiments, hMSCs were used between passages 4 and 8.

2.4.2. hMSCs culture on eggshell membranes

ESM (~10 mm diameter) were sterilized by a wash in 1× phosphate-buffered saline (PBS; Medicago) and then subjected to UV light (Philips, Pila, Poland) on both sides. Then, ESM was washed again with PBS and incubated in 48-well plates until dry before the cells were seeded. hMSCs suspension containing 8000 cells in 50 μL of the medium was slowly dropped onto the outer surface of each membrane and incubated for 1 h at 37 °C. As a control group, hMSCs were seeded onto the surface of non-mineralized eggshell membranes (hMSCs-ESM). Afterward, 500 μL of fresh medium was added to each well plate. For positive controls of osteogenic differentiation, cells were cultured with osteogenic differentiation medium (ODM) DMEM (Sigma-Aldrich) containing 10 % FBS (Sigma-Aldrich), and 1 % penicillin/streptomycin, L-ascorbate acid (50

μg/mL), β-glycerophosphate (10 mmol/L) and dexamethasone (10 nmol/L). All samples were incubated under a 5 % CO_2 atmosphere at 37 °C. The culture medium was replaced every 2 days, and the ESM were processed for subsequent analysis.

2.4.3. Cell viability

The Live/Dead kit assay (Thermo Fisher Scientific) was used to evaluate cell viability after 7 days in culture, following manufacturer's instructions. Briefly, the membranes were incubated in PBS containing Calcein AM (2 μM) and ethidium homodimer (4 μM) at 37 °C for 30 min to stain live and dead cells, respectively. Images from the samples were observed using a confocal microscope (Leica TCS-SP5) and analyzed with Image J software (v. 1.52i, USA).

2.4.4. Scanning electron microscopy

The hMSC-ESMs and hMSC-mESMs were washed with PBS and fixed with 2.5 % (*w/v*) glutaraldehyde in 0.1 M cacodylate buffer (pH 7.4; Polysciences, Warrington, PA) for 24 h at 4 °C. The samples were then rinsed several times with sodium cacodylate buffer. After fixation, the samples were post-fixed with 1 % w/v osmium tetroxide for 1 h RT, dehydrated in steps with ethanol (50 %, 70 %, 90 %, and 100 %, 15 min each), and dried at the critical point in CO_2 and sputter-coated with gold. The images were examined with an FEI Quanta 400 scanning electron microscope (Oregon, USA) and Zeiss Merlin scanning electron microscope (Carl Zeiss, Germany). The images were processed with ImageJ software.

2.4.5. Cell proliferation

2.4.5.1. Alamar Blue assay. The metabolic activity of cells seeded over the ESM and mESM were assessed by colorimetric Alamar Blue assay (AB; Thermo Fisher Scientific) at different time points, following manufacturer's instructions. The fluorescence intensity was measured using a plate reader (Synergy HT, BIO-TEK) with excitation and emission wavelengths of 530 and 590 nm, respectively. The absorbance data was represented as fold increase to day 0. Experiments were performed in triplicate ($n = 3$).

2.4.5.2. CCK8 cell proliferation detection. Cell Counting Kit 8 assay (CCK8; Abcam) was used to measure the proliferation of cells seeded over the ESM and mESM at different time points, following the manufacturer's instructions. The absorbance values were measured using a plate reader (Synergy HT, BIO-TEK) at 460 nm. This assay is based on the conversion of a water-soluble tetrazolium salt, WST-8, into a formazan dye by cellular dehydrogenases, which is directly proportional to the number of living cells. The resulting colorimetric signal provides insights into cell viability and proliferation dynamics over time. Experiments were performed in triplicate (n = 3).

2.4.6. Immunostaining assay

Cell monolayers and ESM were permeabilized using PBS plus 0.01 % Triton X-100 (Sigma-Aldrich) for 5 min and blocked for 1 h at room temperature with 3 % bovine serum albumin (BSA). Samples were then treated with a primary antibody against Osteopontin (OPN; Santa Cruz Biotechnology, 1:200) or Collagen Type I (COL I; Abcam, 1:200) overnight at 4 °C. AlexaFluor 488-conjugated and 594-conjugated secondary antibodies (Thermofisher, 1:500) were used to incubate the samples for 1 h and they were counterstained with Hoechst. Images were obtained using a Leica TCS-SP5 microscope and analyzed with Image J software.

2.4.7. Measurement of free calcium and phosphate ion concentrations

Cell culture supernatant of the samples cultured using DMEM and ODM was collected at different time points. No pretreatments were required. Calcium ions concentration was measured using the Calcium Colorimetric Assay Kit (Sigma-Aldrich) according to the manufacturer's instructions using a plate reader at 575 nm. Phosphate ions concentration was measured using the QuantiChrom Phosphate Assay Kit (BioAssay Systems) according to the manufacturer's instructions using a plate reader at 620 nm. Experiments were performed in quadruplicate ($n = 4$).

2.4.8. Statistical analysis

All graphed data represent the mean ± standard deviation from at least three experiments. To determine differences between conditions the two-tailed Students *t*-test was used for quantitative biochemistry analysis to determine differences between conditions. *P*-values < 0.001 ($^{***}/^{\#\#\#}$), <0.01 ($^{**}/^{\#\#}$) and <0.05 ($^{*}/^{\#}$) were considered statistically significant in all cases.

3. Results

3.1. Microstructural, physicochemical, and morphological properties of mineralized ESM

The methodological procedure for the crystallization of CaP on pieces of ESM is shown in Fig. 1. The outer surface of the ESM, showing an interwoven fiber structure (Fig. 1a), was covered with the microdroplet containing the reagents inside the crystallization mushroom (Fig. 1b) to achieve the controlled mineralization of the fibers (Fig. 1c). The resulting mESM is composed of a mineral layer of CaP coating the membrane (Fig. 1d). The XRD pattern (15-day mESM 37 °C sample) displays broad diffraction peaks that reflect the nano-crystalline character of the mineral. This phase was identified as carbonated-apatite (Figs. 1e, S2). The most intense peak is located at 2θ = 32–34° and corresponds to the combined (121), (112), (030), and (202) diffraction lines (ICDD: 00-019-0272, COD: 969003552). Two other less intense reflections, located at approximately 25.9° and 39.8° correspond to the (002) and (310) diffraction lines, respectively. In the mESM samples prepared for 1 and 7 days, the intensity of the XRD reflections was negligible. Considering the 15-day samples, the crystallite size determined from the apatite (002) line was 20.05 ± 0.10 nm. The 2D-XRD patterns (Fig. S3) showed continuous diffraction arcs within the Debye-Scherrer ring associated with the (002) reflection (considering 360° φ angle rotation), which indicates a crystal random orientation. The unmineralized ESM displays an XRD pattern characteristic of an amorphous material, with a broad band at 2θ ~15–30° (Fig. 1e).

The unmineralized ESM observed from its outermost surface consists of a network of cross-linked fibers randomly aligned, which can converge perpendicularly to each other creating junctions, or in a parallel direction, increasing their thickness (Fig. 2, A1). The width of the fibers varies from 500 nm up to 2 μm, and present well-defined borders and veined texture. The fibers contain mammillary knobs of various sizes (from ~100 nm to 1 μm) on their surface (Fig. 2, A2) [20].

The Raman spectrum of the ESM (Fig. 2, A3) displays an intense narrow band located at 485 cm^{-1}, related to an S—S vibrational mode, associated with disulfide-rich proteins (~10 % cysteine) of the cysteine-rich eggshell matrix proteins (CREMPs) [43,44]. Furthermore, other protein-related intense bands are also identified at 1668 cm^{-1} (amide I), 1240 cm^{-1} (amide III), and 1460 cm^{-1} (CH_2 vibration related to lipids), as well as other less intense bands. On the other hand, the FTIR spectrum of the ESM (Fig. 2, A4) presents several intense peaks related to the organic components, such as amide A at 3272 cm^{-1}; amide I at 1633 cm^{-1}; amide II at 1513 cm^{-1}, and amide III at 1239 cm^{-1} [45]. A detailed description of the ESM Raman and FTIR organic band assignments can be found in Figs. S4a and S5a, respectively. The EDX analyses show a high sulfur concentration (34.5 %) and a low (5.1 %) calcium concentration in the ESM.

The mESM prepared at 25 °C shows the formation of apatite crystals associated with the membrane fiber structure. The mESM prepared at one day (1-day mESM, 25 °C) shows some interfibrillar spaces occluded by mineral precipitate formation (Fig. 2, B1). The deposit consists of

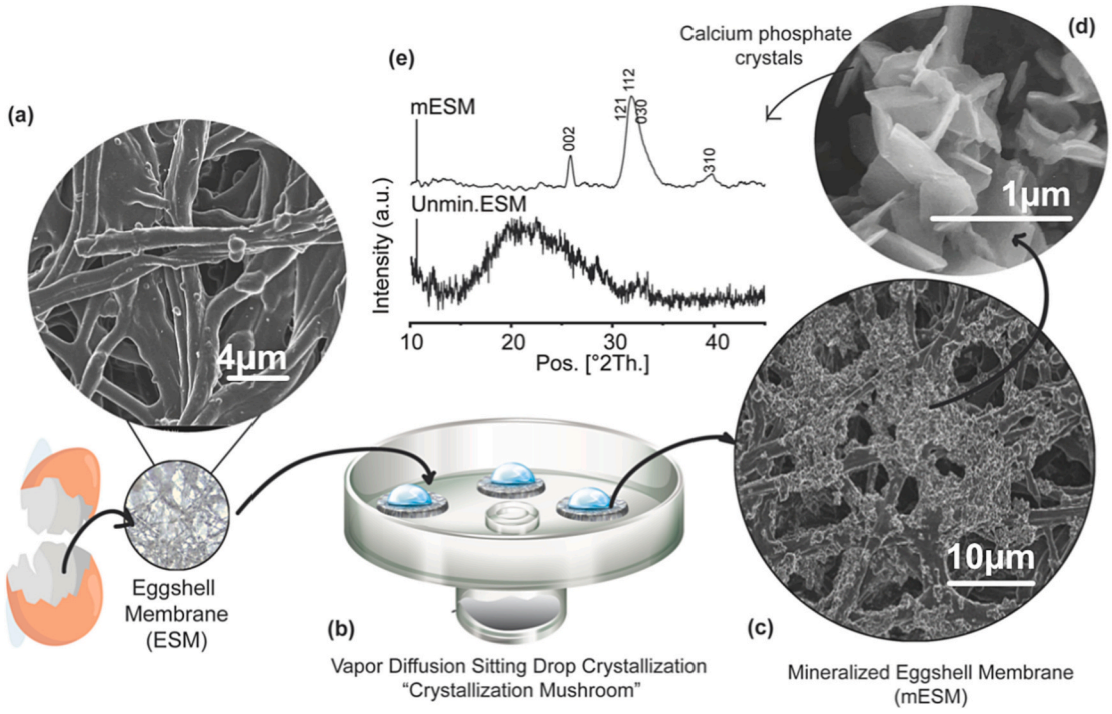

Fig. 1. Methodological set-up for the mineralization of the outer surface of the ESM. (a) Mechanically extracted ESM showing its outermost surface, (b) ESM sections placed on the "crystallization mushroom" device and covered with microdroplets containing calcium and hydrogen phosphate ions, (c) mineralized eggshell membrane (mESM), (d) close-up view of the flake-like crystal morphology (e) XRD patterns corresponding to unmineralized ESM and a mESM biohybrid composite.

flake-like crystals covering the fibers at the zones of the mammillary knobs (Fig. 2, B2). The Raman spectrum a very low-intensity band at 961 cm^{-1} related to the $\nu_1PO_4^{3-}$ vibrational mode of the apatite phase (Fig. 2, B3), combined with several bands associated with the organic components of the membrane [16,46]. In the FTIR spectrum, this sample presents two intense absorption band at 500–600 cm^{-1} (ν_4 PO_4^{3-}) and 900–1200 cm^{-1} (ν_1-ν_3 PO_4^{3-}) (Fig. 2, B4) [47,48]. At longer times (7 and 15 days), the PO_4^{3-} bands increased their intensities while those bands related to the organic components were progressively less detectable (Fig. 2, C3–4: D3–4). In addition, the mESM samples also show a CO_3^{2-} band at ~875 cm^{-1}. The 7-day mESM (25 °C) shows the same flake crystalline morphology as the 1-day mESM (25 °C), but the deposit is thicker with relatively larger crystals (Fig. 2, C1–C2). The Raman spectrum still presents the 961 cm^{-1} apatitic band ($\nu_1PO_4^{3-}$), as well as other organic bands (Fig. 2, C3). The FTIR-ATR spectrum shows the ν_4 PO_4^{3-} and ν_1-ν_3 PO_4^{3-} bands described above (Fig. 2, C4). Finally, at this temperature the 15-days sample shows a remarkable mineral layer (Fig. 2, D1) with crystals presenting a flake-like appearance (Fig. 2, D2). As expected, the 961 cm^{-1} band in the Raman spectrum is more intense than that of the 1 and 7-days samples (Fig. 2, D3). In addition, the PO_4^{3-} vibrational modes continue to be observed in the ATR-FTIR spectrum (Fig. 2, D4).

The ESMs mineralized at 37 °C also show the formation of CaP crystals at 1, 7, and 15 days. The 1-day mESM (37 °C) presents an apparent roughening of the fibers (Fig. 2, E1) and the mineral deposit forms with irregular shapes and the presence of crystalline aggregates of different morphologies (Fig. 2, E2). Moreover, the Raman and FTIR spectra of these samples also display the PO_4^{3-} bands (Fig. 2, E3–E4). The 7-day mESM (37 °C) shows a mineral deposit spread in different zones and partially filling the interfibrillar spaces (Fig. 2, F1). The morphology of these deposits consists of flat-shaped crystals forming flower-like agglomerates (Fig. 2, F2). The PO_4^{3-} bands are also present in both the Raman and FTIR spectra (Fig. 2, F3–F4). The 15-day mESM (37 °C) shows the thicker mineral deposit coating the fibers and almost completely occluding the spaces between the interwoven net (Fig. 2, G1). A close-up view shows semi-circular, flaky, rough deposits merging between them and thickening the membrane fibers (Fig. 2, G2). For this sample the Raman ν_1PO_4 band exhibits the higher relative intensity (Fig. 2, G3). In addition, the FTIR spectrum presents two intense bands at 500–600 cm^{-1} (in the ν_4 PO_4 domain) and 900–1200 cm^{-1} (ν_1–ν_3PO_4) (Fig. 2, G4), along with the bands of organics with lower relative intensity. The deconvolution of the 500–600 cm^{-1} region reveals several sub-bands (Fig. S6, a), the most intense and wide being located at 559 cm^{-1} (Ap, ν_4PO_4), along with other low intensity bands located at 548, 572, and 600 cm^{-1} [46,47]. Three different sub-bands related to hydrogen phosphate vibration (ν_4 HPO_4^{2-}) were also present within the ν_4PO_4 absorption region [46,49]. The ν_1–ν_3 PO_4 region (Fig. S5, b) was deconvoluted in different sub-bands, identified in the apatite, particularly the sub-band at 1020 cm^{-1} which is usually related to non-stoichiometric poorly crystalline apatites [46,49,50]. Moreover, the 1052 cm^{-1} band is related to B-type CO_3^{2-} substitution in the apatite lattice [49]. The band at 984 cm^{-1} is related to PO_4^{3-} in a non-apatitic, non-stoichiometric environment [49], and 1004 cm^{-1} to HPO_4^{2-} vibration modes [46]. An additional deconvolution was performed on the 800–900 cm^{-1} region (Fig. S6, c), revealing three different bands located at 877, 870, and 857 cm^{-1} associated with the $\nu_2CO_3^{2-}$ splitting in the AB-type carbonate substitution of apatite [46,51]. The degree of carbonation was estimated according to Grunenwald et al. [51], comparing the relative intensity of the FTIR ν_2CO_3 carbonate bands relative to the ν_1-ν_3PO_4 phosphate bands. The overall carbonation degree was close to 1 wt%. Finally, EDX analyses in the mESM show Ca and P molar percentages of ~35 % and 21 %, respectively, reaching a Ca/P molar ratio of ~1.65.

Thermogravimetric analyses (Fig. S7) of the ESM show a multi-step thermal decomposition pattern similar to that already reported [52]. In it we can appreciate a first initial weight loss at around 46 °C which is completed at around 130 °C, due to the denaturation of collagen and loss of bound water [16]. A second loss between 230 °C and 500 °C is mainly attributed to the thermal degradation of collagen and glycan chains [53]. The third weight loss, at temperatures between 500 and 550 °C is

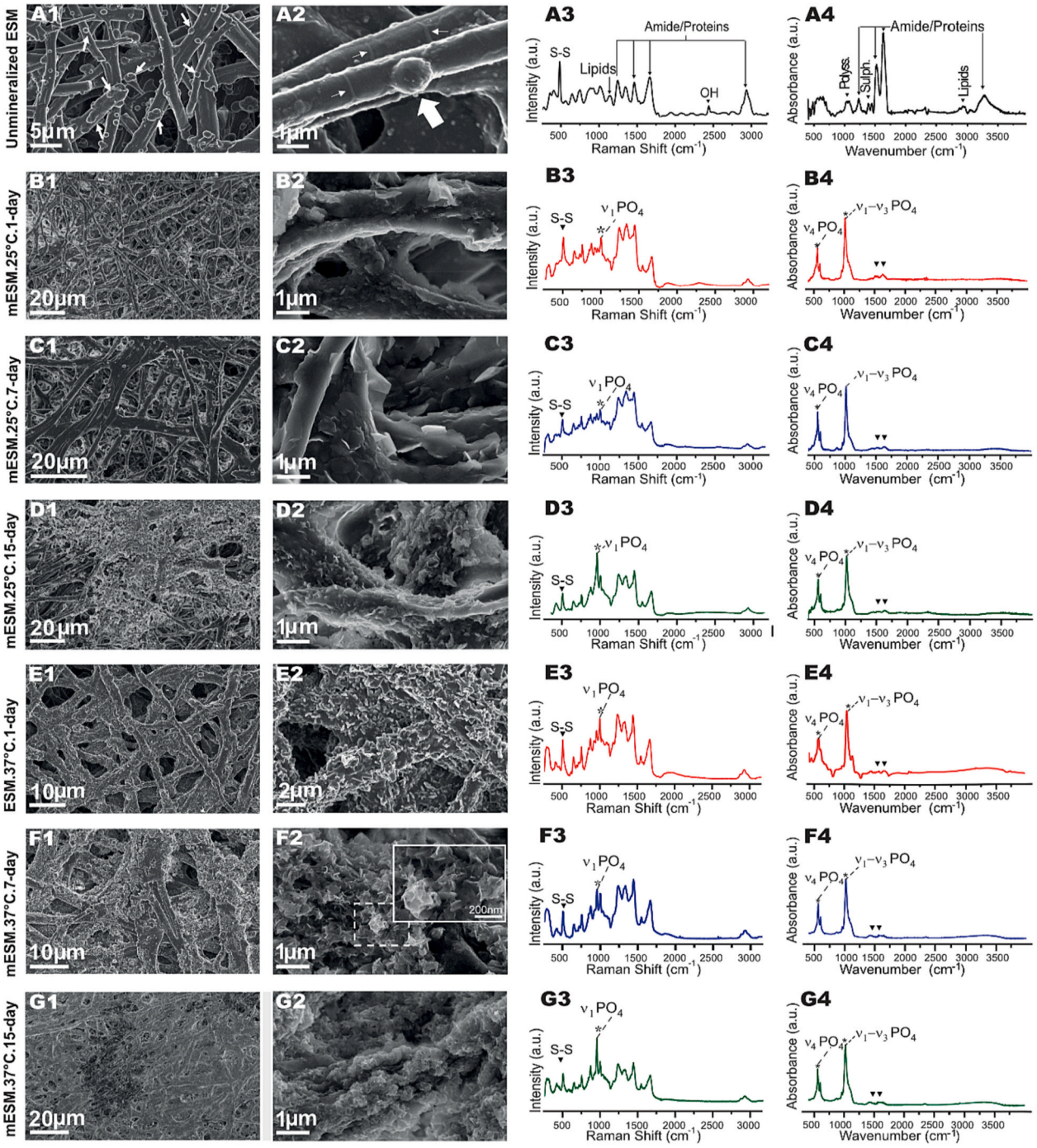

Fig. 2. Characterization of unmineralized ESM and apatite mineralized ESM (mESM) for 1, 7, and 15 days at 25 °C and 37 °C. (A1–A2) SEM micrographs of unmineralized ESM, where the white arrows point to mammillary knobs, and the thinner white arrows in A2 indicate the venous-like structures on the ESM fibers (A3). Raman spectrum of unmineralized ESM, showing the main organic bands: S—S, lipids, and amide bands. (A4) FTIR-ATR spectrum of unmineralized ESM showing the main organic bands: polysaccharides (Polyss.), sulfates (Sulph.), amide, and lipid bands. (B-C-D) Characterization of mESMs prepared at 1, 7, and 15 days at 25 °C (1, 2-SEM images, 3 - Raman spectrum, 4 - ATR-FTIR spectrum). (E-F-G Characterization of mESMs prepared at 1, 7, and 15 days at 37 °C (1, 2-SEM images, 3 - Raman spectra, 4 - ATR-FTIR spectra).

ascribed to the decomposition of the ESM backbone producing the full vaporization without any residue. Compared to the thermogram of the 15 day-mESM 37 °C sample, the loss until 780 °C–840 °C is attributed to the mineral content. Table S1 shows the mineralization percentages were ~4 and 9 wt% for samples at 7 and 15 days 25 °C, and 6, 8.5, and 13.7 wt%, for samples at 1, 7, and 15 days 37 °C, respectively.

XPS characterization allows determining the elemental chemical composition and bonding state of the atoms. The XPS spectrum of the unmineralized ESM (Fig. 3a, bottom; Table S2) displays peaks of O 1s (530 eV), N 1s (399 eV), C 1s (around 284 eV), S 2s (226 eV) and S 2p (162 eV). The O 1s and N 1s belong to functional groups (carboxylic, carbonyl, hydroxyl, amine, amide) of the proteic ESM structure [54], whereas the S 2p and S 2s signals are related to the S—S bond of de disulfide-rich structural proteins that make up the membrane (CREMPS) [43]. The C 1s deconvoluted in three components at 284.6, 285.9, and 287.9 eV related to the C—C, C—N, and C—O bonds of the organic

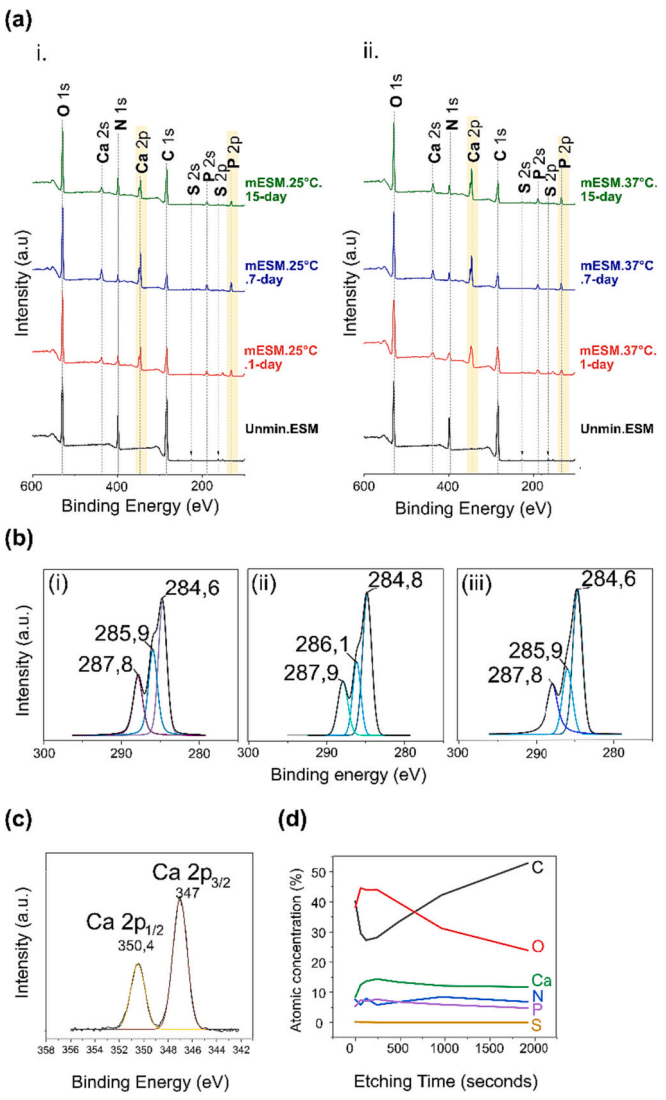

Fig. 3. (a) XPS spectra of unmineralized ESM and mESM at 1, 7 and 15 days (i) at 25 °C and (ii) at 37 °C. (b) C 1s deconvoluted for (i) unmineralized ESM (ii) mESM.25 °C.15-days, and (iii) mESM.37 °C.15-days. (c) inset of Ca 2p, (d) atomic concentration (percentage) *versus* etching time.

groups of the collagen and proteins of the membrane (Fig. 3b, i). These bands slightly shifted for the 25 and 37 °C 15-days mESM samples (Fig. 3b, ii and iii). In addition to those peaks, the XPS spectra of 25 °C (Fig. 3a, i), and 37 °C mESM (Fig. 3a, ii) show those of Ca 2s (438 eV) and Ca 2p (~350 eV), and P 2s (189 eV) and P 2p (132 eV). The Ca 2p is made of two sub-bands, the first one at 347 eV corresponding to Ca 2p 3/2 and the second one at 350 eV corresponding to Ca 2p 1/2 at 350 eV (Fig. 3c). Both are consistent with apatite presence [55]. The C 1s and N 1s of the mESM samples present lower relative intensity than that of Ca and P signals. Here, as the C 1s peak also deconvoluted in three components, we speculate that an additional C source is due to the CH_3COO^- (the reagent) which likely adsorbed on the crystals of the apatite layer [35]. The elemental composition (% at) of ESM and mESM (Table S2) shows Ca/P ratios oscillating between 1.37 and 1.55. Fig. 3d and Table S3 show in addition the depth profile of the elemental composition of the 15 day-mESM 37 °C sample.

The in-depth analysis revealed an abrupt increase in % C while a decrease of % O occurred, in both cases until values are close to those of the ESM substrate. The variation of Ca and P was smoother, with Ca/P ratios 1.56 and 1.67 near the surface of the apatite layer, and up to 2.47 at the highest depth analyzed. This finding indicated the unbalanced Ca and P deposition at the early stages of the CaP layer growth.

3.2. Mechanical properties of mESM

The ESM samples showed thickness values between 0.052 ± 0.003 (group unmineralized ESM) and 0.064 ± 0.006 mm (mESM 37 °C.15-day group). The temperature and mineralization time affected positively the thickness of mESM, especially the mineralization time (Fig. 4a) due to the higher growth of the apatite layer. Regarding the effects of both parameters on the mESM tensile strength, the data showed a greater influence of the mineralization time of the samples compared to the temperature (Fig. 4b).

Experimental data describing the fracture behavior of unmineralized ESM and mESMs are shown in Table 1. The results show that all fracture parameters increase with mineralization time and temperature. The mineralization of the ESM at 37 °C for 15 days produced a significant increase in the elastic modulus and in the total energy absorbed until fracture, represented as the area under the stress-strain curve (Fig. S8). The increase in tensile strength of the mineralized ESM was related to an increase in both values of strain at the proportional limit and of strain at breaking, which led to a greater amount of absorbed energy until failure.

3.3. Cytotoxicity and viability assays on hMSCs

3.3.1. Cell viability determination by confocal microscopy

Cell viability of hMSCs cultured on ESM was tested using the Live/Dead assay and mESM prepared at 37 °C. The results showed that hMSCs adhered to the surfaces of ESM and mESM samples after one day of incubation were viable, presenting a few dead cells. However, the amount of attached live cells was obviously much higher in 7-day and 15-day mESM samples after one day compared with ESM and even after seven days of culture, indicating that mESMs showed good cell survival and can efficiently support hMSCs growth (Fig. 5).

3.3.2. Morphological characterization and cell adherence analysis by SEM

The ESM and mESM seeded with hMSCs were visualized by SEM. Fig. 6 shows the presence of hMSCs attached on the surface of ESM, 7-day mESM and 15-day mESM after 1 and 7 days under standard cell culture conditions. Moreover, in the case of cells grown onto the surface of ESM, they presented a spindle shape in the ESM while became angular with increased cell extensions and a flattened morphology in the mESM surface. These results corroborate the biocompatibility of the mESMs and the good biological properties of the cells in terms of adhesion and spreading.

3.3.3. Evaluation of cell proliferation

The biocompatibility of the samples and cell proliferation were determined using two different colorimetric techniques. On the one hand, the Alamar Blue assay allowed us to monitor the metabolic activity of hMSCs at 1, 5, 10, and 21 days after seeded on ESM, 7 days-mESM, and 15 days-mESM (Fig. 7a). The results revealed a significant increase in cell activity over time in all study groups. Nonetheless, mESM groups showed a greater increase in cell activity than ESM. After 21 days of study under standard cell culture conditions, the observed difference in cell activity between ESM and mESMs groups was statistically significant (Fig. 7a).

On the other hand, cell proliferation was analyzed using the CCK8 assay. For this purpose, samples were cultured and maintained at different time points. The results showed a significant increase in cell viability in all study groups compared to the first day (Fig. 7b). Cell activity in mESM increased compared to the non-mineralized group after 10 days and significantly after 21 days of cell culture.

In essence, these results indicated that the new biomaterial provided a favorable environment for cells and enabled cell proliferation in their different mineralization processes.

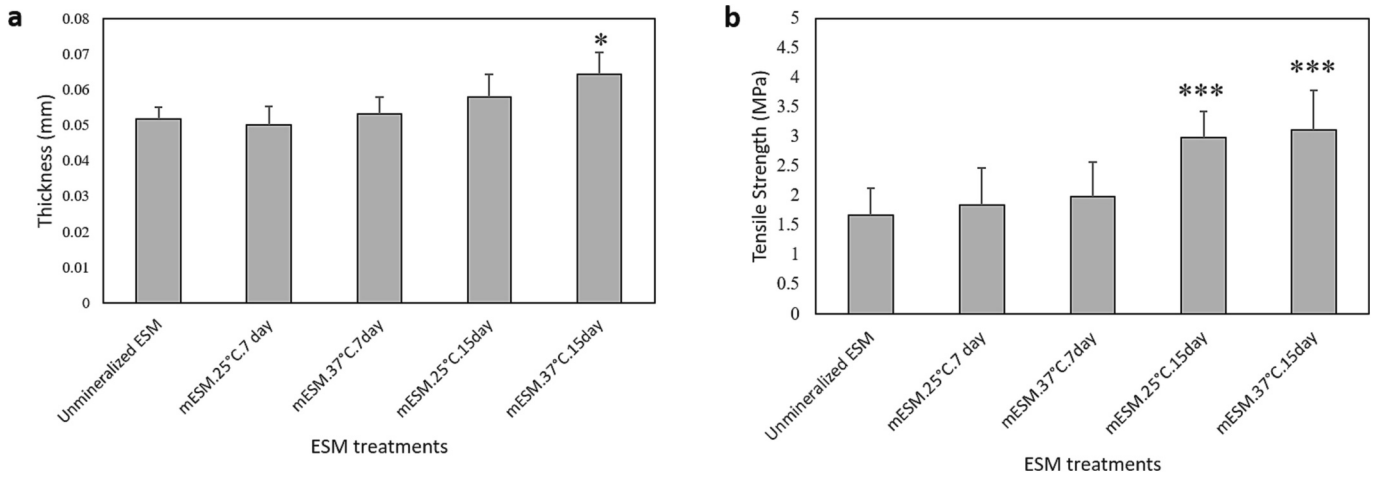

Fig. 4. Values of thickness (a) and tensile strength (b) of unmineralized and mineralized ESM under different conditions (temperature and experimental times). The results are presented as mean and standard deviation ($n = 15$). Statistically significant differences are presented exclusively between unmineralized ESM and mineralized ESM as follows: (*) $p < 0.05$; (**) $p < 0.01$; (***) $p < 0.005$.

Table 1
Mechanical properties of unmineralized ESM and mESMs.

Mechanical properties	Unmineralized ESM	mESM.25 °C. 7 days	mESM.37 °C. 7 days	mESM.25 °C. 15 days	mESM.37 °C. 15 days
Tens. Str. (MPa)	1.67 ± 0.5	1.83 ± 0.6[a]	1.99 ± 0.5[a]	2.98 ± 0.4[b]	3.11 ± 0.6[b]
$\mathcal{E}p$ (%)	23.85 ± 6.9	33.34 ± 9.9[a]	47.01 ± 8.7[b]	48.09 ± 4.7[b]	60.26 ± 6.6[b]
E (MPa)	3.89 ± 1.3	4.05 ± 1.4[a]	5.3 ± 1.7[b]	6.25 ± 1.7[b]	7.06 ± 2.3[b]
$\mathcal{E}u$ (%)	24.96 ± 6.9	36.02 ± 11.5[a]	49.99 ± 10.5[b]	46.22 ± 5.8[b]	57.29 ± 8.6[b]
KIc (J/m^2)	2095.26 ± 1064.4	3731.77 ± 2848.7[a]	4507.19 ± 1783.2[b]	6934.88 ± 1613.1[b]	8141.26 ± 1438.4[b]

Lowercase letter (a) denotes no statistical difference from unmineralized ESM and lowercase letter (b) denotes statistical difference from unmineralized ESM. $\mathcal{E}p$: strain at the proportional limit, *E:* elastic modulus, $\mathcal{E}u$: strain at breaking, and *KIc*: toughness.

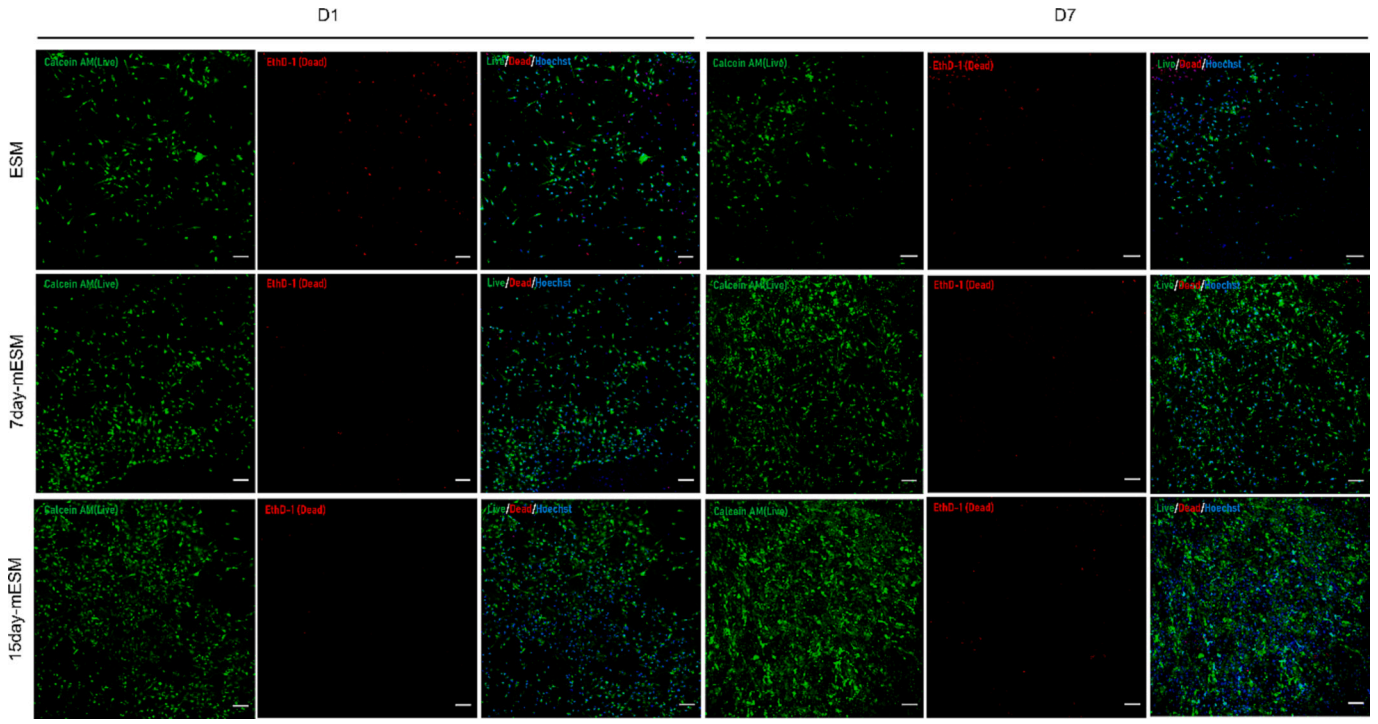

Fig. 5. *In vitro* biocompatibility evaluation of ESM and mESM cultured with hMSCs. Representative confocal images of hMSCs grown in ESM and 7-day and 15-day mESM samples at days 1 and 7 of culture. Live/dead assay was employed, using calcein (green) and ethidium homodimer (red); live cells were stained green, while dead cells were stained red. Cell nuclei were stained blue using DAPI. Scale bars: 100 μm.

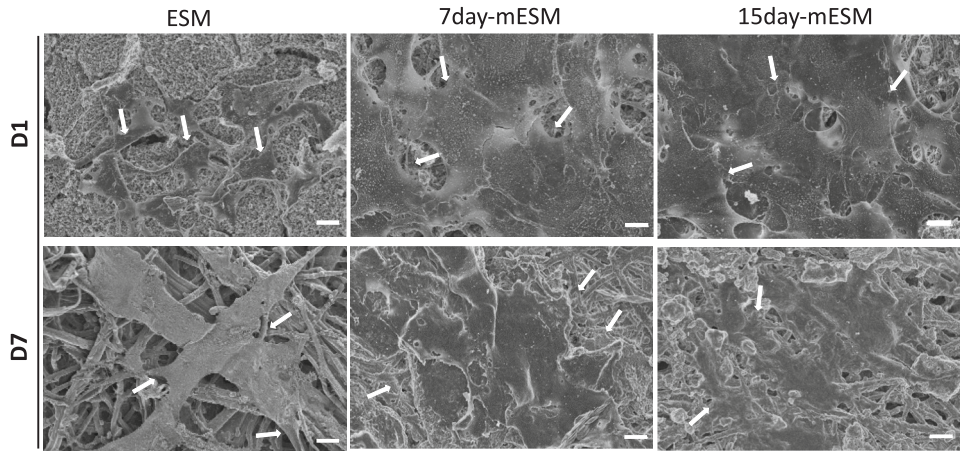

Fig. 6. Scanning electron microscopy (SEM) images of hMSCs on ESM, 7-day and 15 day-mESM samples. Morphology and cell adhesion of hMSCs on mESM after 1 and 7 days of cell culture. White arrows indicate that hMSCs adhered to the material under study. Scale bar: 10 μm. Magnification of 2 K×.

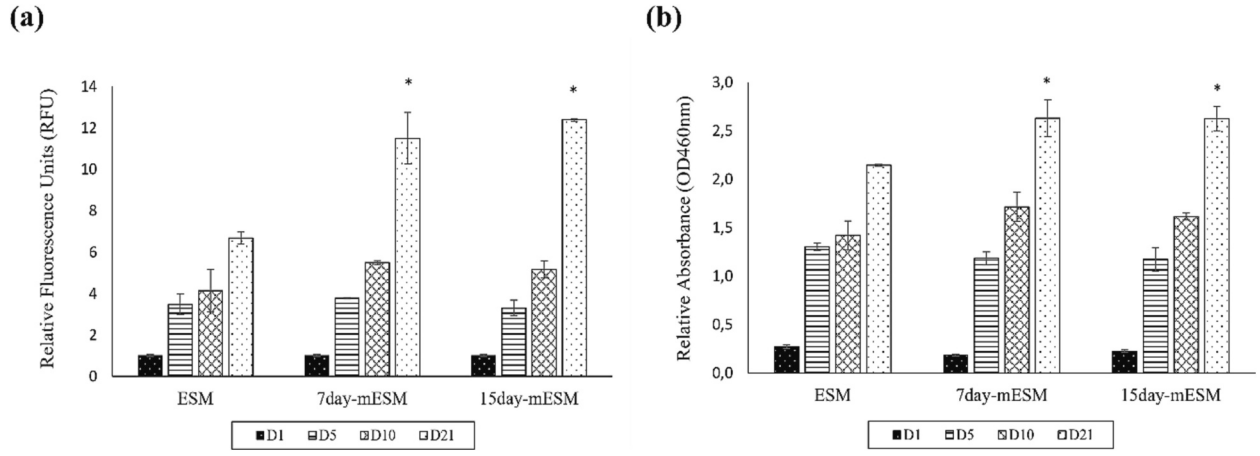

Fig. 7. *In vitro* biocompatibility and cell proliferation evaluation of hMSCs seeded onto ESMs, 7-day mESM, and 15-day mESMs at 1, 5, 10, and 21 days. a) Cell growth measured using Alamar Blue assay; b) CCK8 cell proliferation detection. Data represent the mean ± standard deviation of the significant difference between groups compare to the control group ($n = 3$). (*) $p < 0.05$. (RFU: Relative Fluorescence Units).

3.3.4. Osteogenic characterization hMSCs cultured on ESM and mESMs

Immunofluorescence techniques assessed osteogenic differentiation. Tests were performed using hMSCs under standard cell culture conditions (DMEM) and osteogenically differentiated hMSCs cultured in an osteogenic differentiation medium (hMSCs-OM). Immunofluorescence staining revealed the presence of osteopontin (OPN) and collagen I (COL I) in mESM after 21 days of culture of both hMSCs and hMSCs-OM. The expression of OPN showed a significant increase ($p < 0.005$) in all groups in comparison with the control hMSCs cultured in monolayer (Fig. 8). There was also a significant increase in the presence of OPN between 7-day mESM hMSCs ($p < 0.01$), 7-day mESM hMSCs-OM ($p < 0.05$), 15-day mESM hMSCs ($p < 0.05$), and 15-day mESM hMSCs-OM ($p < 0.005$) with respect to the hMSCs seeded onto the ESM and cultured with a standard medium. The expression of COL I was higher in 15-day mESM hMSCs ($p < 0.01$) and 15-day mESM hMSCs-OM ($p < 0.005$) groups than in control hMSCs cultured in monolayer. In addition, a significant increase in expression of COL I in 15-day mESM hMSC ($p < 0.05$) and 15-day hMSCs-OM ($p < 0.005$) groups compared with hMSCs seeded onto the ESM without osteogenic differentiation medium was observed (Fig. 8). These results indicate that mESM samples are able to induce the differentiation of hMSCs more efficiently than ESM, even without using an osteogenic differentiation medium. Moreover, it was determined if the release of Ca^{2+} or P_i ions is correlated with the differentiation process (Fig. S9). Free Ca^{2+} levels were quantified, and results showed non-significant differences in the samples cultured using DMEM or ODM over time. Nonetheless, there was a trend of decreasing between day 1 and day 10 with a subsequent increase at day 21. However, there was a significant decrease in 7 day-mESM ODM samples in comparison to 7 day-mESM DMEM samples at day 10. On the other hand, no significant differences were observed in the P_i levels between all samples over time but there was an incremental trend in concentration. In addition, there was no relevant variation in the free P_i levels between the same samples cultured with DMEM and ODM except for an increase at day 10 in 15 day-mESM ODM samples in comparison to 15 day-mESM DMEM samples.

4. Discussion

Hybrid biomimetic materials devise applications in several clinical procedures, such as bone regeneration. The development of these biomaterials seeks to replicate the organic-inorganic interactions of highly structured and multifunctional mineralized tissues (*i.e.*, bones and teeth) [56]. Biopolymeric membranes govern some of these interactions and participate in CaP mineralization [3]. In the current study, the pristine ESM was selected as a biopolymeric membrane to explore CaP precipitation by using the VDSD crystallization method. The intrinsic properties of the outer ESM surface, populated of mammillary knobs, are the ones that guide $CaCO_3$ nucleation during eggshell formation [20,57,58] and

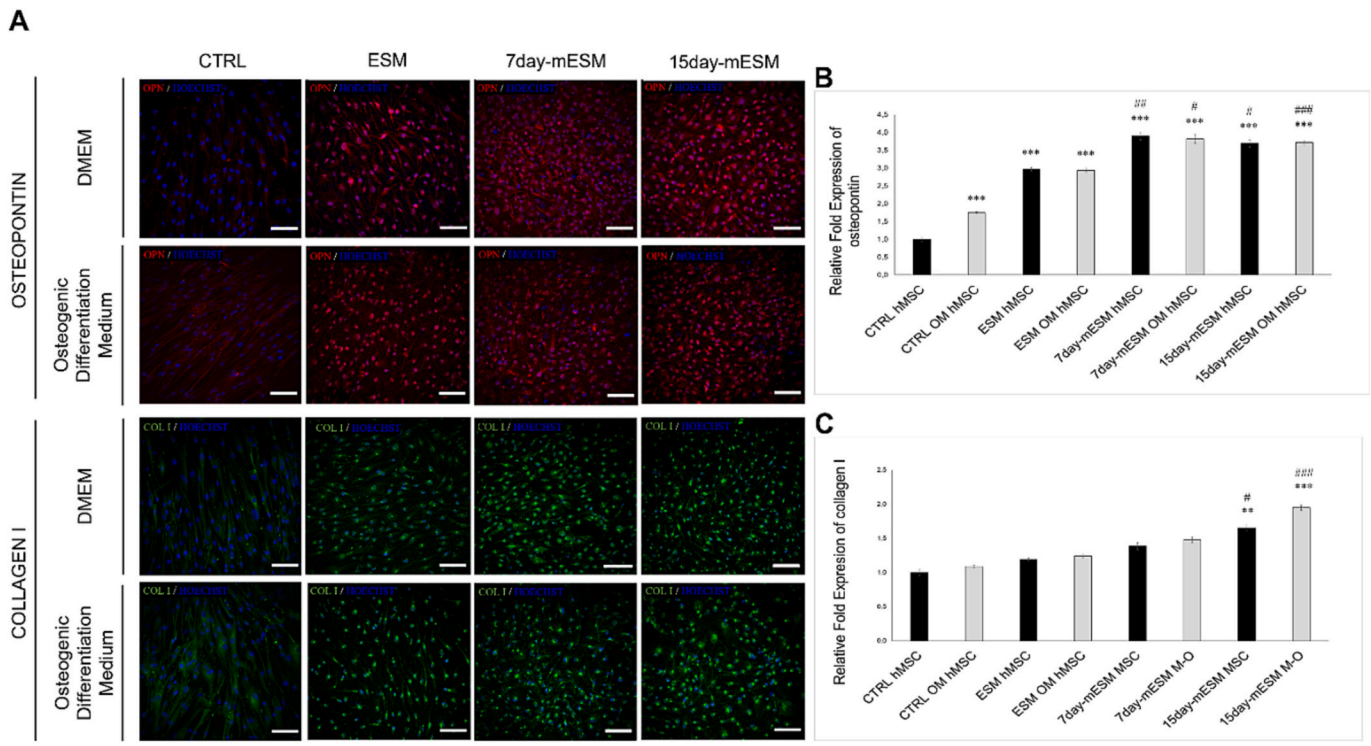

Fig. 8. Osteogenic differentiation potential of ESM and mESM. (A) Immunofluorescence analysis for the detection of OPN and COL I in hMSCs seeded in monolayer (used as control), ESM, or mESM and cultured during 21 days under standard cell culture conditions (DMEM) or in osteogenic differentiation medium (hMSCs-OM). Scale bar: 100 μm. (B) OPN labelling intensity of hMSCs and hMSCs-OM cultured in monolayer, ESM, and mESM. (C) COL I labelling intensity of hMSCs and hMSCs-OM cultured in monolayer, ESM, and mESM. Data represent the mean ± S.D. of the significant difference between groups concerning hMSCs cultured on day 0 ($n = 4$). Significant values are marked with * (comparison with hMSCs cultured in monolayer under standard cell culture conditions) and with # (comparison with hMSCs seeded onto the surface of ESM cultured under standard cell culture conditions); (*/#) $p < 0.05$; (**/##) $p < 0.01$; (***/###) $p < 0.005$.

the ones that have been exploited in this study. Previous studies on CaP mineralization of the ESM were conducted to mineralize both sides of the membrane, *i.e.* Zhang et al. [22], Xu et al. [23], Chen et al. [24]. In these studies, prior the mineralization the ESMs were submitted to acid digestion, which significantly altered the structure of the membrane proteins.

In our study, the crystallographic, morphological, compositional, and vibrational properties of the mESM samples reveal how the outer membrane surface controls CaP precipitation giving rise to the formation of a nanocrystalline apatite coating depicting biomimetic features. The in-depth elemental composition of the CaP coating (mESM 37 °C.15-day sample, Table S3) shows the unbalanced Ca and P content (Ca/P up to 2.47) and the progressive formation of carbonated-apatite with a more stoichiometric composition (Ca/P between 1.56 and 1.67) toward the coating surface. At the same time, a high percentage of organic C in depth and its progressive decrease toward the coating surface can be in part attributed to the presence of free acetate ions adsorbed on the crystals as previously suggested [35], and also to Ca-acetate complexes (the reagent) occluded within the layers. The last event might explain the high Ca/P ratio at the initial stages of the mineral deposition. The presence of N in the coating must be related to N-rich molecules, *i.e.* glycosaminoglycans that likely dissolved from the fibers at the slightly acidic initial pH of the experiments and then adsorbed on the CaP during coating growth.

Additional results of thermogravimetry and thickness of the mESM samples showed the increase of mineral content and thickness with the temperature and mineralization time up to 13.7 ± 3.2 wt% and 0.064 ± 0.006 mm at 37 °C 15 days. These findings reveal the ability of the VDSD technique to tailor mineral content and coating thickness on the outer ESM while protecting the inner layer from mineralization.

An outstanding part of the study has been the characterization of the mechanical properties of mESM, since they determine its performance for potential uses [14]. Previous studies have reported that mechanical properties in biological tissues exhibit a great variability since they depend on their humidity as well as on the heterogeneity and anisotropy of their structure [14,59]. In this respect, to avoid wide variations in the mechanical response, the environmental conditions, the placement of the samples, and the speed of the test were all kept constant. Under these circumstances, our results showed coefficients of variations between 0.2 and 0.3 at a low load application rate, similar to previously reported values [60,61]. The results showed that values of the tensile strength, strain at the proportional limit ($\mathcal{E}p$) and elastic modulus (E) associated to the elastic deformation, as well as the strain at breaking ($\mathcal{E}u$), and toughness (KIc) which are associated to the plastic deformation, all of them increased with the temperature and mineralization times. As the time and temperature increased (mESM 25 °C.15 day and mESM 37 °C.15 day) the stress-strain curves tended to look concave upwards (Fig. S8), which points to a correspondence between the aforementioned increases and the larger values needed for the load to produce strain. This finding suggests the strain at breaking depends on the mineral content and thickness of the mESM.

Our results on the tensile strength of unmineralized ESM are consistent with those from previous reports at the same loading rate [52,62]. Additionally, the tensile strength compares with those of different membranes barriers used in guided/bone tissue regeneration, *i.e.* dry porcine tendon (1.8 MPa) and dry equine bone lamina (1.7 MPa), being also higher to that of dry allogenic collagen (1.3 MPa) [63]. On the other hand, our study showed correspondence between the increase in the tensile strength of mESM and the mineralization percentage of mESM samples. This mechanical behavior would increase the likeliness of mESM being used in applications where membranes with higher tensile strength and elastic modulus are required to maintain their shape without losing the ability to adapt to the defect in bone tissue regeneration procedures [63,64]. Unlike those reported by Torres et al. [14], the

stress-strain curves demonstrated a linear regime, where the strain variation is directly proportional to the variation of stress, without registering a toe region that represents an un-crimping of the membrane.

Nowadays, materials for guided tissue/bone regeneration are mainly synthetic and biological polymer membranes. The functionalization of these membranes with key attributes that satisfies the requirements of mechanical strength and stability, degradation rate, osteogenesis, antibacterial capacity, and clinical manageability, are in the early stages of development [25]. Additives used include proteins, such as bone morphogenetic proteins (BMP) [65], fibrinogen/bredigite [66], cytokines, or nanoparticles, *i.e.*, polysaccharide/bioactive glass nanoparticles [67], or AgNPs [68], which are employed to promote bone regeneration and antibacterial ability of the membranes. Overall, the use of mESM could potentially satisfy some of these requirements.

Biocompatibility is one of the most critical properties a material should possess to be further considered for tissue-engineered applications. Cell functions and behavior can be affected by the topography of the surface to which they adhere [69], so cell viability and adhesion study of the mESM are crucial to determining its effectiveness as a biomaterial. Previous studies have analyzed the biocompatibility of ESM as a biomaterial for wound healing and tissue-engineering applications (further described in [57]). Our results showed that the mineralization affected the functionality of the biomaterial over time, with the microstructure of the mESMs being more advantageous as tissue-engineered materials. Furthermore, the mESMs not only promoted cell proliferation but also favored osteogenic differentiation into hMSCs due to their composition. It is known that the presence of apatite in hMSCs cell culture causes an up-regulation of different osteogenic markers [70]. Our results showed positive expression of the osteogenic markers OPN and COL I in the membranes coated with the apatitic layer. The level of OPN was significantly higher in all groups compared to the hMSC control and significantly higher in mESMs compared to ESMs. On the other hand, the level of COL I was significantly higher in the 15-day mESM groups compared to the control groups in both monolayer and ESM. These results indicate that even in the groups where a standard culture medium was not used, the morphology and mineral content of the membranes appeared to affect in favor of osteogenic differentiation. Therefore, these results demonstrate that the mESM are very useful for guided tissue/bone regenerative medicine treatments since they increase the cytocompatibility and osteoinductive environment on the apatite-mineralized side of the ESM. At the same time, the unmineralized side can act as a barrier to prevent external cell invasion into the bone graft area.

The release of free Ca^{2+} and phosphate ions in ESMs and mESMs was quantified with the intention of determining if the release of Ca^{2+} or P_i ions was correlated with the differentiation process. No significant differences were observed between most groups. However, the immunofluorescence assay showed positive labelling of the main bone tissue proteins in ESM and to a greater extent in mESM. Previously, it has been described by Tanikake et al. [71], that the variation of calcium in the medium might not be a reliable marker even with advancing osteoblastic differentiation of MSCs. Previous studies have described that the release of free Ca^{2+} and P_i ions occurs in CaP formations [72]. Then, the binding of these Ca^{2+} ions with the P_i produced in the biomineralization process promotes osteogenic differentiation into stem cells without the need for any further supplementation [73]. In addition, the characterization of these membranes by immunofluorescence assay agrees with Raman spectra and mineralization results since the composition of ESMs includes phosphate groups that help themselves the osteogenic differentiation of hMSCs. In summary, mESMs present an advantage over ESMs in the increased level of hMSCs osteogenic differentiation induction, thanks to the biomineralization process. Based on our results, we hypothesize that the CaP formed has a more crystalline structure, which makes it more insoluble than amorphous calcium phosphate, and no major variations are observed in the study of the free Ca^{2+} and P_i ions quantified in the samples [73].

The hybrid material (mESM) developed in the current research presents several similarities with the organic matrix and the mineral component of biological tissues. These similarities allow the mineralized ESM to show a specific degree of physicochemical compatibility with calcium phosphate mineralized tissues. These resemblances relate to the organic-inorganic basis of mineralized tissues, the "mild" crystallization conditions (*i.e.*, temperature and pressure close to physiological ones), and the precipitation characteristics of the inorganic phase. The material obtained herein was most likely formed due to mineralization membrane-guided mechanisms that commonly occur in biological systems [10]. The organic components presented in the mineralized biological structures are rich in polyanionic proteins and proteoglycans [57,74]. These biomolecules engage in electrostatic interactions between the anionic domains (*i.e.*, carboxylate, sulfate) that bind to calcium cations of the forming mineral. Indeed, some of these molecules, such as amelogenin (enamel), [75] osteocalcin (bone) [74], and mamillan (ESM) [20], show calcium-binding capacity and have been associated with mineral precipitation in biological tissues. Overall, these interactions constitute an essential trigger for the mineralization process and might have been involved in controlling calcium phosphate precipitation on the ESM. Our results suggest that the outer surface of ESM nucleates a calcium phosphate mineral that mimicked the inorganic phase of mineralized tissues, composed mainly of a carbonated-apatite phase, with non-stoichiometric features and HPO_4^{2-} environments. The mineral phase presents chemical and structural characteristics mimicking those of biological apatite. Furthermore, the methodology presented in this study also constitutes a potential pathway for the sustainable development of biomaterials through the reuse of ESM, a resource considered a waste in the food industry [16].

5. Conclusions

The outer surface of the ESM was mineralized by the SDVD method with a low crystalline, nanosized, carbonated-apatite coating exhibiting biomimetic features while the inner side remained unmineralized. The mineral content and thickness of mESM increased with the experimental temperatures (*i.e.*, 25 °C and 37 °C) and mineralization times from 1 to 15 days. The mechanical properties are closely related to the mineral content of mESM. In addition, mESM also showed *in vitro* osteogenic differentiation and osteoinductive properties. These findings encourage *in vivo* implantation studies to corroborate its potential use in clinical procedures such as guided bone/tissue regeneration in the field of dentistry.

Funding

This work was supported by Ministerio de Ciencia de Innovación (MCI) (Ministry of Science and Innovation, Spain) project PGC2018-102047-B-I00 (MCIU/AEI/FEDER/UE), Fundación Mutua Madrileña, Grant/Award Number: FMM-AP17196-2019, the Instituto de Salud Carlos III, ERDF funds (DTS21/00098), the Consejería de Economía y Universidad, Junta de Andalucía (PYC20 RE 015 UGR; P20_00208 of 2020) and the European Regional Development Fund (ERDF) - Next Generation/EU program and AYUD/2022/33525 (FICYT).

CRediT authorship contribution statement

Conceptualization, J.G.-M., P.A.-L, J.A.M.; Investigation, A.T.-M., P. A.-L., A.V.-M., P.B.E., E.L.-R.; Methodology, A.T.-M., P.A.-L., A.V.-M., P. B.E., E.L.-R; Supervision, J.G.-M.; Writing—original draft preparation, J. G.-M., P.A-L., A.T.-M. E.L.-R., J.A.M; Writing—review and editing, J.G.-M., P.A-L., J.A.M; Funding acquisition, J.G.-M., E.L.-R., J.A.M. All authors have read and agreed to the published version of the manuscript.

Declaration of competing interest

The authors applied for a patent at the Oficina Española de Patentes y Marcas on 28/04/2022. Ref. P202230390 and for PCT patent at European Patent Office on 28/04/2023, Ref. PCT/ES2023/070274.

Data availability

Data will be made available on request.

Acknowledgements

This work has been awarded with the Spanish Institute for Egg Studies Research Award (2023). We are grateful for the assistance of Raquel Fernandez Penas from Laboratory of Crystallographic Studies and the technical staff of both the Scientific Instrumentation Center (University of Granada) and the Scientific and Technical Services (University of Oviedo). Adriana Torres Mansilla gratefully acknowledges her credit of studies from Ministerio de Ciencia, Tecnología e Innovación de Colombia (MinCiencias).

Appendix A. Supplementary data

Supplementary data to this article can be found online at https://doi.org/10.1016/j.bioadv.2023.213605.

References

[1] C. Gillman, A. Jayasuriya, FDA-approved bone grafts and bone graft substitute devices in bone regeneration, Mater. Sci. Eng: C. 130 (2021), 112466, https://doi.org/10.1016/j.msec.2021.112466.
[2] A. Greenwald, S. Boden, V. Goldberg, Y. Khan, C. Laurencin, R. Rosier, Bone-graft substitutes: facts, fictions, and applications, J. Bone Jt. Surg. 83 (2001) S98–103, https://doi.org/10.2106/00004623-200100022-00007.
[3] A. Veis, J. Dorvee, Biomineralization mechanisms: a new paradigm for crystal nucleation in organic matrices, Calcif. Tissue Int. 93 (2013) 307–315, https://doi.org/10.1007/s00223-012-9678-2.
[4] S. Khan, M. Ul-Islam, M.W. Ullah, Y. Zhu, K.B. Narayanan, S.S. Han, J.K. Park, Fabrication strategies and biomedical applications of three-dimensional bacterial cellulose-based scaffolds: a review, Int. J. Biol. Macromol. 209 (2022) 9–30, https://doi.org/10.1016/j.ijbiomac.2022.03.191.
[5] M. Zhang, F. Zhang, C. Li, H. An, T. Wan, P. Zhang, Application of chitosan and its derivative polymers in clinical medicine and agriculture, Polymers. 14 (2022), https://doi.org/10.3390/polym14050958.
[6] N. Maaruf, N. Jusoh, Angiogenic and osteogenic properties of fibrin in bone tissue engineering, Malays. J. Med. Health Sci. 18 (2022) 85–94.
[7] M. Filippi, G. Born, M. Chaaban, A. Scherberich, Natural polymeric scaffolds in bone regeneration, Front. Bioeng. Biotechnol. 8 (2020) 474, https://doi.org/10.3389/fbioe.2020.00474.
[8] C. Combes, S. Cazalbou, C. Rey, Apatite biominerals, Minerals. 6 (2016) 34, https://doi.org/10.3390/min6020034.
[9] C. Drouet, Apatite formation: why it may not work as planned, and how to conclusively identify apatite compounds, Biomed. Res. Int. 2013 (2013), e490946, https://doi.org/10.1155/2013/490946.
[10] S. Mann, Biomineralization: Principles and Concepts in Bioinorganic Materials Chemistry, Oxford University Press, New York, 2001.
[11] J. Currey, Hierarchies in biomineral structures, Science. 309 (2005) 253–254, https://doi.org/10.1126/science.1113954.
[12] J. Gómez-Morales, M. Iafisco, J.M. Delgado-López, S. Sarda, C. Drouet, Progress on the preparation of nanocrystalline apatites and surface characterization: overview of fundamental and applied aspects, Prog. Cryst. Growth Charact. Mater. 59 (2013) 1–46, https://doi.org/10.1016/j.pcrysgrow.2012.11.001.
[13] A. Rodríguez-Navarro, P. Marie, Y. Nys, M. Hincke, J. Gautron, Amorphous calcium carbonate controls avian eggshell mineralization: a new paradigm for understanding rapid eggshell calcification, J. Struct. Biol. 190 (2015) 291–303.
[14] F. Torres, O. Troncoso, F. Piaggio, A. Hijar, Structure–property relationships of a biopolymer network: the eggshell membrane, Acta Biomater. 6 (2010) 3687–3693.
[15] J. Arias, M. Fernandez, J. Dennis, A. Caplan, Collagens of the chicken eggshell membranes, Connect. Tissue Res. 26 (1991) 37–45, https://doi.org/10.3109/03008209109152162.
[16] M. Baláž, Eggshell membrane biomaterial as a platform for applications in materials science, Acta Biomater. 10 (2014) 3827–3843, https://doi.org/10.1016/j.actbio.2014.03.020.
[17] Y. Shi, K. Zhou, D. Li, V. Guyonnet, M. Hincke, Y. Mine, Avian eggshell membrane as a novel biomaterial: a review, Foods. 10 (2021) 2178, https://doi.org/10.3390/foods10092178.
[18] D. Carrino, J. Dennis, T. Wu, J. Arias, M. Fernandez, J. Rodriguez, J. Fink, A. Heuer, A. Caplan, The avian eggshell extracellular matrix as a model for biomineralization, Connect. Tissue Res. 35 (1996) 325–329, https://doi.org/10.3109/03008209609029207.
[19] M. Wong, M. Hendrix, K. von der Mark, C. Little, R. Stern, Collagen in the eggshell membranes of the hen, Dev. Biol. 104 (1984) 28–36, https://doi.org/10.1016/0012-1606(84)90033-2.
[20] A. Rao, M. Fernández, H. Cölfen, J. Arias, Distinct effects of avian egg derived anionic proteoglycans on the early stages of calcium carbonate mineralization, Cryst. Growth Des. 15 (2015) 2052–2056, https://doi.org/10.1021/acs.cgd.5b00342.
[21] Y. Nys, J. Gautron, J. Garcia-Ruiz, M. Hincke, Avian eggshell mineralization; biochemical and functional characterization of matrix proteins, C. R. Palevol. 3 (2004) 549–562, https://doi.org/10.1016/j.crpv.2004.08.002.
[22] Y. Zhang, Y. Liu, X. Ji, C. Banks, J. Song, Flower-like agglomerates of hydroxyapatite crystals formed on an egg-shell membrane, Colloids Surf. B: Biointerfaces 82 (2011) 490–496, https://doi.org/10.1016/j.colsurfb.2010.10.006.
[23] Z. Xu, K. Neoh, A. Kishen, A biomimetic strategy to form calcium phosphate crystals on type I collagen substrate, Mater. Sci. Eng. C. 30 (2010) 822–826, https://doi.org/10.1016/j.msec.2010.03.014.
[24] X. Chen, L. Zhu, W. Wen, L. Lu, B. Luo, C. Zhou, Biomimetic mineralisation of eggshell membrane featuring natural nanofiber network structure for improving its osteogenic activity, Colloids Surf. B: Biointerfaces 179 (2019) 299–308, https://doi.org/10.1016/j.colsurfb.2019.04.009.
[25] Y. Gao, S. Wang, B. Shi, Y. Wang, Y. Chen, X. Wang, E. Lee, H. Jiang, Advances in modification methods based on biodegradable membranes in guided bone/tissue regeneration: a review, Polymers. 14 (2022) 871, https://doi.org/10.3390/polym14050871.
[26] M. Wieckiewicz, K. Boening, N. Grychowska, A. Paradowska-Stolarz, Clinical application of chitosan in dental specialities, Mini Rev. Med. Chem. 17 (2017) 401–409.
[27] I. Elgali, O. Omar, C. Dahlin, P. Thomsen, Guided bone regeneration: materials and biological mechanisms revisited, Eur. J. Oral Sci. 125 (2017) 315–337, https://doi.org/10.1111/eos.12364.
[28] J. Arias, A. Gonzalez, M. Fernandez, C. Gonzalez, D. Saez, J. Arias, Eggshell membrane as a biodegradable bone regeneration inhibitor, J. Tissue Eng. Regen. Med. 2 (2008) 228–235, https://doi.org/10.1002/term.87.
[29] L. Dupoirieux, D. Pourquier, M. Picot, M. Neves, Comparative study of three different membranes for guided bone regeneration of rat cranial defects, Int. J. Oral Maxillofac. Surg. 30 (2001) 58–62, https://doi.org/10.1054/ijom.2000.0011.
[30] E. Calciolari, F. Ravanetti, A. Strange, N. Mardas, L. Bozec, A. Cacchioli, N. Kostomitsopoulos, N. Donos, Degradation pattern of a porcine collagen membrane in an in vivo model of guided bone regeneration, J. Periodontal Res. 53 (2018) 430–439, https://doi.org/10.1111/jre.12530.
[31] A. Torres-Mansilla, E. Delgado-Mejía, Influence of separation techniques with acid solutions on the composition of eggshell membrane, Int. J. Poult. Sci. 16 (2017) 451–456, https://doi.org/10.3923/ijps.2017.451.456.
[32] H. Khalid, A. Chaudhry, 4 - basics of hydroxyapatite—structure, synthesis, properties, and clinical applications, in: A.S. Khan, A.A. Chaudhry (Eds.), Handbook of Ionic Substituted Hydroxyapatites, Woodhead Publishing, 2020, pp. 85–115, https://doi.org/10.1016/B978-0-08-102834-6.00004-5.
[33] J. Gómez-Morales, C. Verdugo-Escamilla, J. Gavira, Bioinspired calcium phosphate coated mica sheets by vapor diffusion and its effects on lysozyme assembly and crystallization, Cryst. Growth Des. 16 (2016) 5150–5158, https://doi.org/10.1021/acs.cgd.6b00716.
[34] J. Gómez-Morales, L. González-Ramírez, C. Verdugo-Escamilla, R. Fernandez-Penas, F. Oltolina, M. Prat, G. Falini, Induced nucleation of biomimetic nanoapatites on exfoliated graphene biomolecule flakes by vapor diffusion in microdroplets, Crystals. 9 (2019) 341, https://doi.org/10.3390/cryst9070341.
[35] M. Iafisco, J. Gómez-Morales, M. Hernández-Hernández, J. García-Ruiz, N. Roveri, Biomimetic carbonate–hydroxyapatite nanocrystals prepared by vapor diffusion, Adv. Eng. Mater. 12 (2010) B218–B223, https://doi.org/10.1002/adem.201080003.
[36] G. Ramírez-Rodríguez, J. Delgado-López, J. Gómez-Morales, Evolution of calcium phosphate precipitation in hanging drop vapor diffusion by in situ Raman microspectroscopy, CrystEngComm. 15 (2013) 2206–2212, https://doi.org/10.1039/C2CE26556G.
[37] M. Fernandez, K. Passalacqua, J. Arias, J. Arias, Partial biomimetic reconstitution of avian eggshell formation, J. Struct. Biol. 148 (2004) 1–10, https://doi.org/10.1016/j.jsb.2004.05.003.
[38] K. John, Biocompatibility of dental materials, Dent. Clin. N. Am. 51 (2007) 747–760, viii, https://doi.org/10.1016/j.cden.2007.03.003.
[39] D. Williams, On the mechanisms of biocompatibility, Biomaterials. 29 (2008) 2941–2953, https://doi.org/10.1016/j.biomaterials.2008.04.023.
[40] B. Cullity, S.R. Stock, Elements of X-ray Diffraction, 3rd ed., Pearson Education Ltd, Essex, UK, 2014, p. 245 (ISBN: 978-1-292-04054-7).
[41] J. Strnková, Š. Nedomová, V. Kumbár, J. Trnka, Tensile stength of the eggshell membranes, Acta. Univ. Agric. Silvic. Mendelianae. Brun. 64 (1) (2016) 159–164, https://doi.org/10.11118/actaun201664010159.
[42] A.S.T.M. Standard, Standard test method for tensile properties of thin plastic sheeting, in: Annual Book of ASTM standards (D882–88), ASTM International, Conshohocken, United States, 2012, https://doi.org/10.1520/D0882-12. Updated August 15, 2018.

[43] V. Kodali, S. Gannon, S. Paramasivam, S. Raje, T. Polenova, C. Thorpe, A novel disulfide-rich protein motif from avian eggshell membranes, PLoS One 6 (2011), https://doi.org/10.1371/journal.pone.0018187.
[44] Z. Movasaghi, S. Rehman, I. Rehman, Raman spectroscopy of biological tissues, Appl. Spectrosc. Rev. 42 (2007) 493–541, https://doi.org/10.1080/05704920701551530.
[45] A. Barth, Infrared spectroscopy of proteins, Biochim. Biophys. Acta 1767 (2007) 1073–1101, https://doi.org/10.1016/j.bbabio.2007.06.004.
[46] C. Rey, O. Marsan, C. Combes, C. Drouet, D. Grossin, S. Sarda, Characterization of calcium phosphates using vibrational spectroscopies, in: Advances in Calcium Phosphate Biomaterials, Springer, Berlin, Heidelberg, 2014, pp. 229–266, https://doi.org/10.1007/978-3-642-53980-0_8.
[47] C. Rey, M. Shimizu, B. Collins, M. Glimcher, Resolution-enhanced Fourier transform infrared spectroscopy study of the environment of phosphate ions in the early deposits of a solid phase of calcium-phosphate in bone and enamel, and their evolution with age. I: investigations in the upsilon 4 PO_4 domain, Calcif. Tissue Int. 46 (1990) 384–394, https://doi.org/10.1007/BF02554969.
[48] C. Rey, M. Shimizu, B. Collins, M. Glimcher, Resolution-enhanced fourier transform infrared spectroscopy study of the environment of phosphate ion in the early deposits of a solid phase of calcium phosphate in bone and enamel and their evolution with age: 2. Investigations in thev3 PO4 domain, Calcif. Tissue Int. 49 (1991) 383–388, https://doi.org/10.1007/BF02555847.
[49] H. Ou-Yang, E. Paschalis, A. Boskey, R. Mendelsohn, Two-dimensional vibrational correlation spectroscopy of in vitro hydroxyapatite maturation, Biopolymers. 57 (2000) 129–139, https://doi.org/10.1002/(SICI)1097-0282(2000)57:3<129::AID-BIP1>3.0.CO;2-O.
[50] F. Ren, Y. Leng, Carbonated apatite, type-a or type-B? KEM. 493–494 (2011) 293–297, https://doi.org/10.4028/www.scientific.net/KEM.493-494.293.
[51] A. Grunenwald, C. Keyser, A. Sautereau, E. Crubézy, B. Ludes, C. Drouet, Revisiting carbonate quantification in apatite (bio)minerals: a validated FTIR methodology, J. Archaeol. Sci. 49 (2014) 134–141, https://doi.org/10.1016/j.jas.2014.05.004.
[52] H. Gharibi, A. Abdolmaleki, Thermo-chemical modification of a natural biomembrane to induce mucoadhesion, pH sensitivity, and anisotropic mechanical properties, J. Mech. Behav. Biomed. Mater. 87 (2018) 50–58, https://doi.org/10.1016/j.jmbbm.2018.07.014.
[53] M. Molavian, A. Abdolmaleki, H. Gharibi, K. Tadavani, M. Zhiani, Safe and green modified ostrich eggshell membranes as dual functional fuel cell membranes, Energ Fuel 31 (2) (2017) 2017–2023, https://doi.org/10.1021/acs.energyfuels.6b02546.
[54] G. Da Silva, C. Araújo, A. Gonsalves, Evaluation of eggshell membrane as an alternative biopolymeric matrix for delivery of nimesulide, Rev. Colomb. Cienc. Quim. Farm 50 (2) (2021) 550–570, https://doi.org/10.15446/rcciquifa.v50n2.91038.
[55] Y. Ho, K. Man, S. Joshi, V. Mangesh, M. Pantawane, T. Wu, Y. Yang, N. Dahotre, In-vitro biomineralization and biocompatibility of friction stir additively manufactured AZ31B magnesium alloy-hydroxyapatite composites, Bioact. Mater. 5 (4) (2020) 891–901, https://doi.org/10.1016/j.bioactmat.2020.06.009.
[56] C. Wang, K. Jiao, J. Yan, M. Wan, Q. Wan, L. Breschi, J. Chen, F. Tay, L. Niu, Biological and synthetic template-directed syntheses of mineralized hybrid and inorganic materials, Prog. Mater. Sci. 116 (2021), 100712, https://doi.org/10.1016/j.pmatsci.2020.100712.
[57] J. Gautron, L. Stapane, N.L. Roy, Y. Nys, A. Rodriguez-Navarro, M. Hincke, Avian eggshell biomineralization: an update on its structure, mineralogy and protein tool kit, BMC Mol. Cell Biol. 22 (2021) 11, https://doi.org/10.1186/s12860-021-00350-0.
[58] Y. Li, Y. Li, S. Liu, Y. Tang, B. Mo, H. Liao, New zonal structure and transition of the membrane to mammillae in the eggshell of chicken Gallus domesticus, J. Struct. Biol. 203 (2018) 162–169, https://doi.org/10.1016/j.jsb.2018.04.006.
[59] M. Garrido, M. Elices, C. Viney, J. Pérez-Rigueiro, The variability and interdependence of spider drag line tensile properties, Polymer 43 (2002) 4495–4502, https://doi.org/10.1016/S0032-3861(02)00254-9.
[60] K. Miller, K. Chinzei, Mechanical properties of brain tissue in tension, J. Biomech. 35 (2002) 483–490, https://doi.org/10.1016/s0021-9290(01)00234-2.
[61] K. Miller, K. Chinzei, Constitutive modelling of brain tissue; experiment and theory, J. Biomech. 30 (11/12) (1997) 1115–1121, https://doi.org/10.1016/S0021-9290(97)00092-4.
[62] H. Choi, Y. Kim, J. Suh, J. Han, Beneficial effect on rapid skin wound healing through carboxylic acid-treated chicken eggshell membrane, Mater. Sci. Eng. C 128 (2021), 112350, https://doi.org/10.1016/j.msec.2021.112350.
[63] J. Caballé-Serrano, A. Munar-Frau, L. Delgado, R. Pérez, F. Hernández-Alfaro, Physicochemical characterization of barrier membranes for bone regeneration, J. Mech. Behav. Biomed. 97 (2019) 13–20, https://doi.org/10.1016/j.jmbbm.2019.04.053.
[64] H. Wachtel, S. Fickl, M. Hinze, W. Bolz, T. Thalmair, The bone lamina technique: a novel approach for lateral ridge augmentation—a case series, Int J Periodontics Restorative Dent 33 (4) (2013) 491–497, https://doi.org/10.11607/prd.1248.
[65] M. Du, T. Zhu, X. Duan, S. Ge, N. Li, Q. Sun, P. Yang, T., Acellular dermal matrix loading with bFGF achieves similar acceleration of bone regeneration to BMP-2 via differential effects on recruitment, proliferation and sustained osteodifferentiation of mesenchymal stem cells, Mater. Sci. Eng. C Mater Bio Appl. 70 (2017) 62–70, https://doi.org/10.1016/j.msec.2016.08.049.
[66] M. Kouhi, V. Reddy, M. Fathi, M. Shamanian, A. Valipouri, S. Ramakrishna, Poly (3-hydroxybutyrate-co-3-hydroxyvalerate)/fibrinogen/bredigite nanofibrous membranes and their integration with osteoblasts for guided bone regeneration, J. Biomed. Mater. Res. Part A. 107 (2019) 1154–1165, https://doi.org/10.1002/jbm.a.36607.
[67] J. Rodrigues, N. Alves, J. Mano, Biomimetic polysaccharide/bioactive glass nanoparticles multilayer membranes for guided tissue regeneration, RSC Adv. 6 (2016) 75988–75999, https://doi.org/10.1039/C6RA14359H.
[68] J. Wang, L. Zhan, X. Zhang, R. Wu, L. Liao, J. Wei, Silver nanoparticles coated poly (L-lactide) electrospun membrane for implant associated infections prevention, Front. Pharmacol. 11 (2020) 431, https://doi.org/10.3389/fphar.2020.00431.
[69] D. Kim, Y. Gwon, S. Park, W. Kim, K. Yun, J. Kim, Eggshell membrane as a bioactive agent in polymeric nanotopographic scaffolds for enhanced bone regeneration, Biotechnol. Bioeng. 118 (2021) 1862–1875, https://doi.org/10.1002/bit.27702.
[70] P. Sutthavas, P. Habibovic, S.H. van Rijt, The shape-effect of calcium phosphate nanoparticle based films on their osteogenic properties, Biomater. Sci. 9 (2021) 1754–1766, https://doi.org/10.1039/D0BM01494J.
[71] Y. Tanikake, M. Akahane, A. Furukawa, Y. Tohma, Y. Inagaki, T. Kira, Y. Tanaka, Calcium concentration in culture medium as a nondestructive and rapid marker of osteogenesis, Cell Transplant. 26 (6) (2017) 1067–1076, https://doi.org/10.3727/096368916X694166.
[72] H. Pan, X. Liu, R. Tang, H. Xu, Mystery of the transformation from amorphous calcium phosphate to hydroxyapatite, Chem. Commun. (Camb.) 46 (39) (2010) 7415–7417, https://doi.org/10.1039/c0cc00971g.
[73] P. Wolint, L. Näf, D. Schibler, N. Hild, W. Stark, P. Giovanoli, M. Calcagni, J. Buschmann, Suspension of amorphous calcium phosphate nanoparticles impact commitment of human adipose-derived stem cells in vitro, Biology (Basel) 10 (2021) 7, 675, https://doi.org/10.3390/biology10070675.
[74] S. Rees, D. Wassell, R. Waddington, G. Embery, Interaction of bone proteoglycans and proteoglycan components with hydroxyapatite, Biochim. Biophys. Acta (BBA) Gen. Subj. 1568 (2001) 118–128, https://doi.org/10.1016/S0304-4165(01)00209-4.
[75] B. Tarasevich, C. Howard, J. Larson, M. Snead, J. Simmer, M. Paine, W. Shaw, The nucleation and growth of calcium phosphate by amelogenin, J. Crystal Growth. 304 (2007) 407–415, https://doi.org/10.1016/j.jcrysgro.2007.02.035.